Surface Zn enrichment induced by excimer laser annealing in ZnO nanorods

I. Carlomagno[a], I. Lucarini[b], V. Secchi[*b], F. Maita[c], D. Polese[c], S. Mirabella[e,f], G. Franzò[e], A. Notargiacomo[d], G. Di Santo[a], S. Gonzalez[a], L. Petaccia[a], L. Maiolo[c]

[a]*Elettra Sincrotrone Trieste, Basovizza (TS), Italy*
[b]*Dipartimento di Scienze, Università Roma Tre, Rome - Italy*
[c]*CNR-IMM Rome, Italy*
[d]*CNR-IFN Rome, Italy*
[e]*CNR-IMM, Catania, Italy*
[f]*Dipartimento di Fisica e Astronomia, Università di Catania, Catania, Italy*

Abstract

ZnO nanorods (NRs) play a crucial role in the manufacturing of electronic and optical devices and sensors. Using complementary techniques, we explore how their optical and conductive performances can be improved by Excimer Laser Annealing (ELA) at 75 and 100 mJ/cm^2. Our data show that ELA induces the melting and re-crystallization of the NRs surface, resulting into the reduction of the average crystallite size and lattice parameter of the system and suggesting a partial transition towards metallic Zn. The increase of Zn and the removal of oxygen defects at the surface are compatible with photoelectron spectroscopies (UPS and XPS) data and explain the enhancement of the UV/visible emission ratio observed in photoluminescence. The ELA also affects the in-plane electrical conductivity: the carriers mobility improves up to 4 times depending on the laser energy density. Our results demonstrate that ELA is effective in tuning the surface properties of ZnO NRs affecting the Zn concentration at the surface and removing some oxygen defects. The combination of these two effects results into the improvement of the optical and electrical responses of the systems.

Keywords: ZnO nanorods, laser annealing

1. Introduction

Laser irradiation as a fast and local heating treatment represents the most efficient alternative in devices processing to conventional thermal procedures for a plethora of bulk and nanostructured materials [1]. Laser techniques span over a large range of wavelengths (from UV to infrared) and powers, allowing a rapid change in the morphology of materials and inducing a vast variety of phenomena such as standard heating, recrystallization, densification, ablation, etc. [2, 3]. Additionally, considering the specific absorption coefficient of a material, it is possible to concentrate the radiation absorption and the consequent heating in a very narrow region of a stack of different layers, thus confining the thermal budget without damaging the underlying films. This feature results particularly important for those devices directly fabricated on polymeric substrates for the implementation of high performing flexible electronics [4, 5, 6, 7].

Among different types of laser treatments, the excimer laser annealing (ELA) is an irradiation process commonly applied in semiconductors and device processing, since the UV wavelength has a strong interaction with a number of materials including silicon, germanium, gallium nitride, silicon carbide, and zinc oxide allowing material recrystallization, defects removal and doping activation [8]. ELA has been successfully used in flexible electronics both as a technique to improve semiconductors quality [9] and as a smart detaching method to release the polymer from a rigid carrier made in glass [10]. Especially for polysilicon and indium gallium zinc oxide based thin film transistors, ELA has provided superior properties in terms of material's electrical mobility and crystalline quality, limiting in any case the total thermal budget usually needed to achieve such performances [11, 12]. This argument is even more valid for semiconductor nanostructures, where the intrinsic high surface/volume ratio favors the heat transfer, triggering deep changes in the material morphology and band gap [13, 14]. Semiconducting metal oxides (MOs) nanostructures make no exception: indeed, ELA has been already applied to ZnO nanorods and nanowires [15, 16], TiO$_2$ nanoporous films [17, 18], and even more complex MOs nanoalloys to tune the optical and electrical properties of these materials. In particular, ELA seems to be able to provide deep changes in ZnO nanostructures allowing at the same time its implementation on polymeric substrates, thus opening the way to manufacture wearables and highly sensitive sensors where ZnO acts as the active material [17].

ZnO nanostructures can be obtained with relatively easy and low-cost processes such as chemical bath deposition (CBD) or sol-gel method, producing a plethora of different nanostructures at temperature below 100°C [19, 20, 21, 22]. These methods, however, also produce defect energy levels in the bandgap, causing severe persistent photocurrent (PPC) phenomena (from

---

hours to days), thus limiting the implementation of this material as optical or gas sensor operating at low temperature (even room temperature) [23].

ELA is known to be effective in controlling the concentration of defects in ZnO thin films [24] and to enhance the system performances in terms of photoluminescence (PL) reponse and decrease in resitivity [25]. The mechanisms underlying the ELA-induced modifications are complex and include several effects. Previous research on ZnO nanorods explained the enhanced UV emission as due to a higher crystalline quality and to the increase of oxygen vacancies [26]. However, it is known that in ZnO nanostructures the origin of the PL is not due to the oxygen vacancies [27, 28]. According to a recently proposed model, the increase in surface conductivity and the enhanced UV emission are originated from a higher concentration of Zn interstitials (Zn_i) [29]. This interpretation agrees with what typically observed on ZnO thin films and simple nanostructures but, to our knowledge, it has never been backed by experimental observations of ZnO nanorods electronic properties. Indeed, shedding light on this mechanism would be particularly important to explain empirical results obtained on room temperature gas sensors based on laser-annealed ZnO nanorods [30] and to propose alternative procedures to maximize device sensitivity or methods to discriminate specific analytes interactions.

In this work, we assess ELA-induced effects on ZnO nanorods by finely studying the underlying physical processes. Combining different techniques, we propose an extensive analysis through a multi-scale approach to explain how laser irradiation affects the optical and electrical properties of the nanorods. To this end, we probe the shallow valence levels near the Fermi energy as well as the deeper core levels by Ultraviolet Photoemission Spectroscopy (UPS) and X-ray Photoemission Spectroscopy (XPS), respectively. The defects population inside the gap was investigated through PL measurements. Scanning Electron Microscopy (SEM) and Grazing Incidence X-ray Diffraction (GIXD) were employed to explore changes in the morphology and in the long-range crystalline order of the ZnO nanorods. Finally, the electrical conductivity of the material was analysed via transmission line measurement (TLM) and electrochemical measurements.

2. Sample preparation

ZnO nanorods were grown by chemical bath deposition on a 0.5 μm thick silicon oxide layer thermally grown on a ligthly doped Si wafer. To trigger the nanostructures growth a precursor layer of ZnO diluted in ethanol was used. The details of the growth procedure can be found in [31]. After the ZnO nanorods growth, the samples were loaded in a vacuum chamber equipped with stepping motors for laser irradiation. An excimer ultraviolet laser with a wavelength $\lambda = 308$ nm was operated choosing a rectangular beam (1 x 60 mm^2) with a Gaussian beam profile at a frequency of 10 Hz and 5 shots per point. We explored two energy densities: 75 and 100 mJ/cm^2. For values above 150 mJ/cm^2, we observed the flattening of the nanostructures and a partial film ablation.

3. Experimental details

The morphological analysis of the samples was carried out by SEM using a Zeiss EVO MA10 SEM at an accelerating voltage of 10 kV. Images were collected at normal incidence (top view, i.e. 0° sample tilt) and at 50° sample tilt (1). SEM view of cleaved samples borders at a 90° sample tilt allowed for a statistical analysis of the NWs length by averaging over at least 35 samples while the standard deviation was taken as the measurement error. The average height calculated for the pristine, 75, and 100 mJ/cm^2 samples resulted to be $h_0 = 0.60 \pm 0.15$ μm, $h_{75} = 0.35 \pm 0.11 \mu m$, $h_{100} = 0.21 \pm 0.10 \mu m$, respectively.

The long range order was explored by GIXD. Data were collected at the MCX beamline at Elettra Sincrotrone Trieste [32], using an incident photon energy of 8 keV, and with an incidence angle of 4.0° and 0.75°, resulting into an attenuation length of the X-ray beam of 2 μm and 500 nm, respectively. The use of different angular geometries allows one to assess different depths of the sample, thus providing a measure of the homogeneity of the crystalline arrangement along the depth. PL measurements were carried out by pumping at around 1 mW with the 325 nm line of a HeCd laser chopped through an acousto-optic modulator at a frequency of 55 Hz. The PL signal was analyzed by a single grating monochromator, detected by a photomultiplier and recorded with a lock-in amplifier using the acousto-optic frequency as a reference.

In order to evaluate the conductivity of the samples, TLM and Impedance Spectroscopy were carried out. For TLM, Al contacts were lithographically patterned on the ZnO NRs and the current flowing between the contacts was tested at room temperature by using a Karl Suss probe station. The contact resistance of Al on ZnO was neglected[33]. Impedance spectroscopy analysis was performed by using a potentiostat Verstatat4 by PAR. Two samples having the same surface area were selected as working electrode, one with the as deposited ZnO NRs and the second with the specimen laser annealed at 100 mJ/cm^2. The testing chamber, filled with a KCl solution 0.1 M, was sealed with an Au Counter Electrode and a Pt Reference Electrode, measuring the impedance from 0.1 Hz up to 10 KHz.

Photoelectron spectroscopies are extremely surface sensitive: henceforth, impurities and adsorbed species can produce relevant changes to the spectra. To reduce these contributions, before the measurements the samples were kept at 120 °C for 30 min to let adsorbed water molecules desorb from the surface. SR-XPS measurements were carried out at the SuperESCA beamline at Elettra Sincrotrone Trieste[34]. The samples were loaded in a UHV chamber with a base pressure in the 10^{-9} mbar range. The photocurrent generated on the first optic element of the beamline (a mirror placed upstream to the measurement chamber) was used to normalize each spectrum. The energy was calibrated setting the Au 4f peak from a reference Au foil to 84.0 eV. The pass energy was set to 10 eV, while the incident photon energy was set to optimise the photoemission signal for the ranges of Zn 2p (hν = 1150 eV) and O 1s (hν = 650 eV). This choice also resulted in a similar electron mean free path for the two ranges (around 0.7 nm), leading to a probing depth of
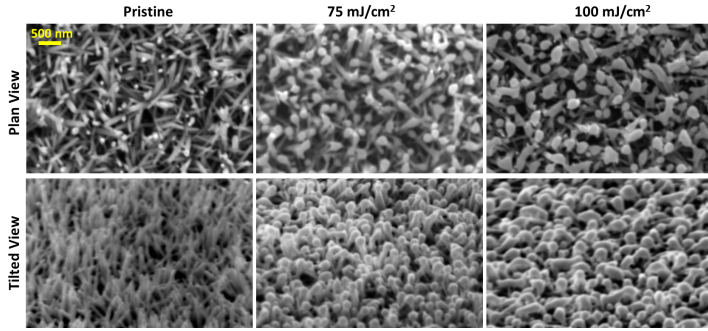
Figure 1: SEM images for pristine (a), 75 mJ/cm^2 (b), and 100 mJ/cm^2 irradiated samples (c) in top view (top row) and tilted view (bottom row)

$2 \div 3$ nm. UPS measurements were carried out at the BaDElPh beamline at Elettra, Trieste[35]. Using an exciting radiation of 31 eV, photoelectrons were collected in normal emission in the binding energy range $2 \div 14$ eV, with a pass energy of 5 eV. The kinetic energies of the photoelectrons correspond to a probing depth of about $2 \div 3$ nm, i.e. comparable to that of XPS. The Binding Energies were calibrated with respect to the Fermi edge measured, in the same analyzer conditions, on clean polycrystalline Cu. For each sample, 10 consecutive spectra were collected and then averaged.

4. Results and discussion

4.1. Morphology and structure: SEM and XRD

SEM images are shown in Fig.1: those collected after laser irradiation show a rounder shape of the NRs tips which, in some areas, are fused with one another. This suggests that the laser heats the topmost part of the NRs, resulting into the melting of the NRs tips and their further re-solidification in a smoother surface.

The tilted view SEM investigation shows that upon ELA tretaments at 75 mJ/cm^2 and 100 mJ/cm^2 the height of the pristine sample ($h_0 = 0.60 \pm 0.15 \ \mu$m) has a consistent and monotonic decrease ($h_{75} = 0.35 \pm 0.11 \ \mu$m and $h_{100} = 0.21 \pm 0.10 \ \mu$m). This reduction, together with the tips melting, indicates an increase in the density of the ZnO layer. Such findings can anticipate some major effects in the photoelectron spectroscopies. In particular, the smoother surface is expected to minimize the shadowing effect for the XPS and UPS signals.

To shed light on the crystalline nature of the NRs, especially upon the melting-solidification process, GIXD was used. Diffraction patterns were recorded at two different incidence angles ($\theta = 0.75°$ and $\theta = 4.0°$) to exploit different surface sensitivities and hence distinguish the surface effects from the global ones. The diffraction patterns were recorded in a wide 2θ range extending from 30° to 70° and showed the typical peaks of wurtzite structure for all the samples (see Supporting Information Fig.1). The two incidence geometries show similar peaks positions, indicating that the wurtzite arrangement is found in the whole NRs layer. Small discrepancies can be better appreciated considering a small 2θ range, as reported in Fig.2 for $\theta = 0.75°$ (top panel) and $\theta = 4.0°$ (bottom panel).

In both geometries, the (002) peak appears to be the most intense both before (black solid line) and after the laser irradiation (75 mJ/cm^2 red dashed, and 100 mJ/cm^2 blue dotted line). This points to a preferential orientation along the c-axis. Upon laser irradiation, the intensities of the three features get closer to one another. This is observed for both geometries, i.e. it affects the whole ZnO layer. Such effect can be originated from the partial loss of the preferential orientation of some facets and/or from the removal of vacancies in the lattice [36] possibly occurring during the melting and recrystallization of the material suggested by the SEM observations.

For a better comparison of the diffraction patterns recorded for the pristine sample in the two different geometries, grey lines were drawn in Fig.2 at the angular positions corresponding to the (100), (200), and (101) diffraction peaks observed in the most grazing geometry. Compared to the $\theta = 0.75°$ geometry, the positions found at higher incidence appear slightly shifted towards higher angles ($2\theta_{0.75°} - 2\theta_{4.0°} = 0.08°$), indicating that the average lattice parameter is smaller at the tips of the NRs. The same is observed upon laser annealing: the lattice parameter of irradiated samples is smaller in the tips region.

Upon ELA, the peaks in Fig.2 are found to shift towards higher angles by $\simeq 0.1°$: this is clearly visible at $\theta = 0.75°$ whereas it is not observed at $\theta = 4.0°$. This suggests that the recrystallization determines a contraction of the lattice parameter in the shallow region of the ZnO. A similar shift was already attributed to release of some residual stress in the material, and/or to the removal of some surface oxygen [37, 36], and, although too small to be interpreted as the transition of Zn from oxidized to metallic phase [38], it could indicate the first stages of such transition, or the transition involving a limited amount of the investigated region. Such surface enrichment in Zn supports the model proposed by Kaupuzs et al. which attributes to the laser-induced temperature gradient the origin of the Zn$_i$ drift towards the surface [29].

Also, the annealing results into the broadening of the peaks which, again, is more evident at $\theta = 0.75°$ while it is barely noticeable on the 002 peak collected at $\theta = 4.0°$. The peaks broadening indicates a reduction in size of the diffraction domains and can be related to smaller crystallites size. Such reduction was quantified using the Scherrer's equation[39] and resulted to be around 30% upon both irradiation processes, going from 50 nm (pristine) to about 35 nm (both irradiated samples).

4.2. Optical properties: Photoluminescence

The optical properties of the ZnO NRs were explored through the analysis of the PL spectra, reported in Fig.3. Two main features can be observed: a sharp peak in the UV range (around 3.3 eV, i.e. 380 nm) and a broad, less intense feature in the visible range. The latter extends in a wide region and is made up of at least two contributions: a green component (2.23 eV) originated from oxygen vacancies at the surface, and an orange component (2.03 eV) related to O vacancies in the bulk [28].

Upon irradiation, the samples present an increased emission in the UV and a damped response in the visible range: both effects are heavier for the 100 mJ/cm^2 irradiation. The PL intensity increase in the UV can be explained with the Zn$_i$ dif-
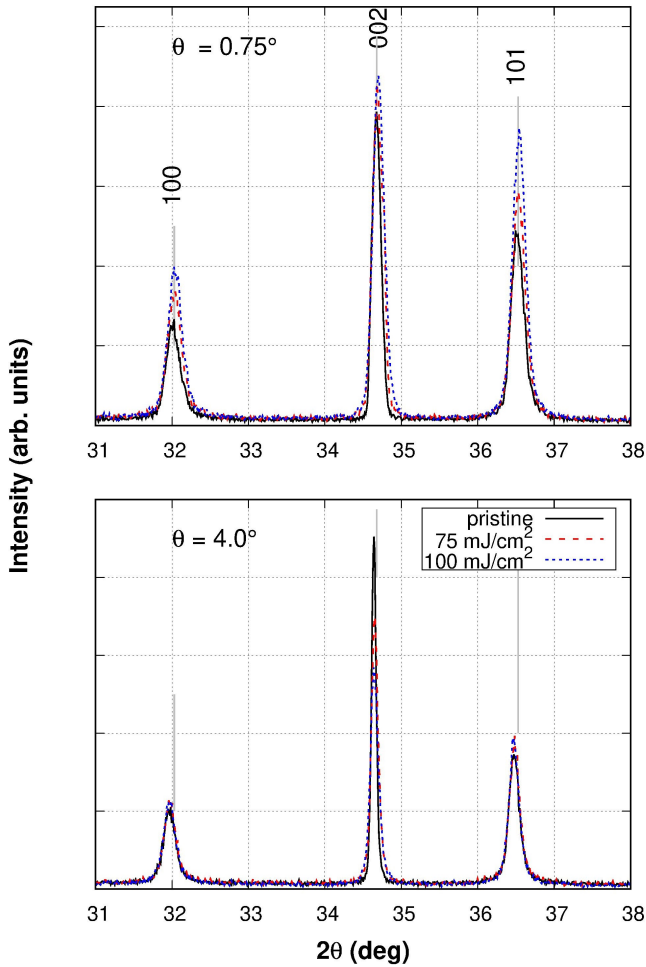
Figure 2: XRD patterns collected in grazing incidence for the pristine (black solid line) and irradiated samples at 75 (red dashed) and 100 mJ/cm² (blue dotted line). The top panel shows the XRD pattern collected with 0.75° incidence, the bottom one at 4.0°. The grey lines serve as a reference to highlight the shift of the peaks.

Figure 3: Photoluminescence emission of the three samples. Inset: I_{UV}/I_{vis} ratio for the three samples.

4.3. Charge transport properties

The effect of laser annealing on the samples conductivity was investigated by TLM and impedance spectroscopy. During the TLM, in addition to the current due to the intrinsic conductivity of the samples, i_0, a persistent photocurrent, i_{ppc}, was observed. The persistent photocurrent is induced by the ambient light in the measuring room and its decay might take hours. In order to get rid of the i_{ppc}, the TLM were carried out several hours after the light was switched off, i.e. until the i_{ppc} had completely decayed. From i_0, the conductivity was then calculated as:

$$\sigma = \frac{i_0}{\Delta V} \cdot \frac{l}{s} \qquad (1)$$

where $\Delta V = 10$ V, $l = 50$ μm is the distance between the electrodes, and $s = d \cdot h$ is the NR surface crossed by the current, i.e. the length of the electrodes $d = 200$ μm multiplied by the NRs average height. The values are reported in Tab.1. We must stress here that, for a proper conductivity assessment via TLM, both the porous nature and the density evolution of the ZnO layer upon laser irradiation must be taken into account. However, considering these details would complicate the analysis making it highly time demanding. Therefore, we neglected the variations of porosity and density and proceeded for a mere qualitative evaluation of the conductivity which should be intended as an "effective conductivity". As shown in Tab.1, upon laser irradiation, the effective conductivity increases by three orders of magnitude.

The increase in σ can be explained with ELA-induced migration of Zn_i towards the surface region [29] and with the decrease in surface defects with consequent enhancement in free-electron mobility [41]. In facts, these shallow donors could compensate the electron accumulation layer at the surface which is known to heavily affect the electrical properties of the ZnO devices [44, 41].

fusion to the surface, as proposed recently[29]. However, this process alone cannot account for the evolution of the visible emission. The visible PL of ZnO nanostructures is originated mostly from surface defects [40, 41] whose energy levels lie in the middle of the gap. The strong increase in the I_{UV}/I_{vis} ratio, shown in the inset of Fig.3, indicates that the laser annealing reduces the population of the defects [42]. It should be noted that UV and visible emissions in ZnO occur at different lifetimes, much shorter for UV than for visible [43], pointing out that the photo-generated carriers recombine faster in UV emission, while for visible photons the recombination process is slower. The ELA treatment clearly induces a modification of the ZnO crystal leading to a polycristalline materials with smaller grain size. The presence of grain boundaries represents a non radiative recombination path for electron-hole pairs, and such a concomitant process will affect much more the slower process (visible emission).
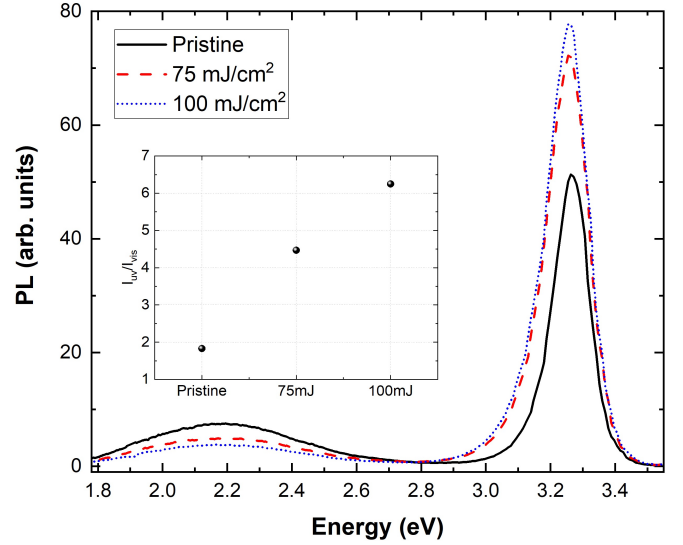
4

Table 1: Average height of the ZnO NRs as from the SEM measurements h, current flowing between the electrodes during the TLM measurements i_0, and effective conductivity σ for each sample estimated through TLM measurements.

	h	i_0	σ
	(μm)	(μA)	$(\Omega \cdot cm)^{-1}$
pristine	0.60	0.5	0.2
75 mJ/cm^2	0.35	50	$3.6 \cdot 10^2$
100 mJ/cm^2	0.21	50	$6.0 \cdot 10^2$

Table 2: Results obtained from Impedance Spectroscopy, using a Randles circuit accounting for: the resistance of the solution, Re, the charge transfer resistance, Rct, and the double layer capacity, Qdl.

	Re	Rct	Qdl	a
	(Ω)	$(k\Omega)$	(μF)	
pristine	357.8	443.2	2.2	0.7
100 mJ/cm^2	225.3	99.5	6.7	0.6

In order to achieve a quantitative assessment of the conductive properties of the samples, impedance spectroscopy was used. Indeed, simple electrical measurements on the samples (i.e. TLM testing method) could not take into account material density differences and the high contribution of the surface of the nanostructures, making incorrect the usage of the Ohm's second law in the resistivity calculation. Impedance spectroscopy highlighted a four times higher impedance for the as grown ZnO nanostructure at low frequency, strengthening the assumption of a significant contribution of the surface states to the conduction (see Fig.4. Additionally, a simple Randles model (inset of Fig.4) has been used to explain the behaviour of the material for the two morphologies, obtaining similar results (see the table 2). The differences evaluated in the resistance of the solution (Re) can be ascribed to minimal variations in the distance among the electrodes in testing chamber.

4.4. Electronic structure: XPS and UPS

In order to understand the effects of the ELA in terms of modifications to the electronic properties of the system, XPS and UPS were used. Both these techniques are highly surface sensitive, hence they are ideal to detect even small variations in the electronic properties related to surface alterations. In our case, the experimental parameters were set so to assess only the topmost $2 \div 3$ nm.

4.4.1. XPS

The Zn 2p region presents two peaks around 1021 and 1044 eV attributed to Zn 2p$_{3/2}$ (shown in the Supporting Information in Fig.2) and Zn2 p$_{1/2}$, respectively [45, 46, 47]. The laser irradiation results into a higher intensity for both peaks with a larger effect for the higher laser fluency. Such increase can be partly due to the smoother surface leading to a smaller shadowing effect, and it is also compatible with a higher concentration of Zn at the surface. Details about the disentanglement of these two effects are reported below. A shift of 0.15 eV towards lower binding energies is observed upon the 100 mJ/cm^2 treatment. This finding confirms the evolution of the system towards a more metallic-like nature as suggested from GIXD
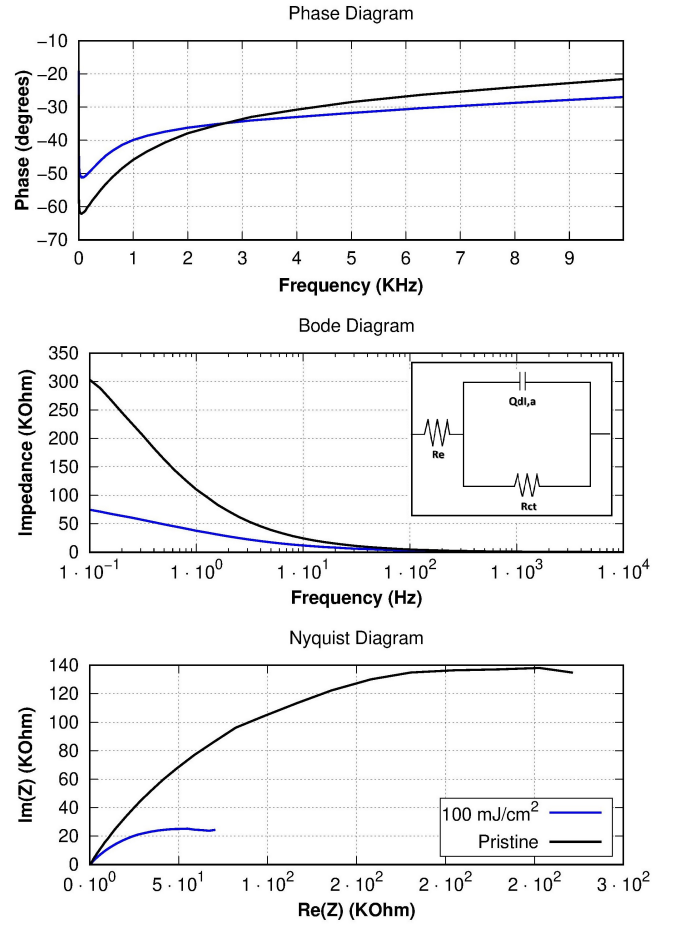

Figure 4: Phase diagram, Bode plot, and Nyquist diagram for the two samples from 0.1 Hz up to 10 KHz. At low frequency, the impedance of the as grown material is four times higher respect the laser annealed one, demonstrating the contribution of the surface states to the conduction for the laser annealed sample. Inset: simple Randles circuit for the extraction of the parameters of the equivalent model.

data. A similar effect, previously attributed to the surface lattice oxygen desorption [48], is compatible with a higher concentration of Zn$_i$ in the surface region of the NRs as suggested by the GIXD and previously proposed by [29]. The absence of energy shift or peak asymmetry upon the 75 mJ/cm^2 laser irradiation indicates that this treatment does not generate a temperature gradient being high enough to produce a detectable effect. The dependence of the Zn$_i$ thermal drift on the laser fluence was already discussed in [29].

In the O 1s region, the XPS spectra present a complex feature that was fitted using 3 contributions as shown in Fig.5. The three component are:

- O$_a$: around 530.0 eV, ascribed to Zn-O[49, 50, 51, 52];

- O$_b$: around 531.5 eV, attributed to surface O in the O sublattice or from oxocarbons or carbohydrate compounds[28]

- O$_c$: around 532.5 eV, from adsorbed molecules (O$_2$, CO$_2$, H$_2$O...) [53, 54, 28]

Table 3: Energy positions and relative intensities of the O 1s components obtained from the best fit procedures, and O/Zn intensity ratio.

	Energy (eV)	Rel. Int. (%)	O/Zn ratio
pristine	530.2	40	
	531.5	42	0.17
	532.6	18	
75 mJ/cm^2	530.1	46	
	531.3	36	0.11
	532.3	18	
100 mJ/cm^2	530.1	44	
	531.3	37	0.10
	532.3	19	

The energy positions of the peaks and their relative intensities, obtained from the best fit procedures (shown in Fig.5) are reported in Table 3. The general intensity of the complex feature was found to increase upon ELA. As discussed in the case of Zn 2p, this increase can be due to the lower shadowing effect produced by the more regular surface morphology and/or to the variation of the surface stoichiometry. However, while the morphology evolution would affect both Zn and O peaks equally, a different stoichiometry would result in the increase of only one of them. Therefore, to disentangle the two effects, one can calculate the O/Zn intensity ratio. To eliminate the contribution of oxygen species not related to the ZnO, only the O$_a$ contribution was taken into account for the oxygen intensity. As reported in the last column of Table 3, the initial value calculated for the pristine sample, decreases upon the ELA treatments. This indicates that a Zn enrichment is definitely occurring within the depth probed by XPS.

The energy positions of the three components show a shift upon ELA: the O$_a$ component, linked to the ZnO, is found at 0.1 eV towards lower binding energies, compatible with the shift found in Zn 2p core level. The O$_b$ and O$_c$ components are also shifted by -0.2 and -0.3 eV, respectively.

The relative intensity of O$_c$ is unchanged upon laser irradiation, indicating that the relative amount of adsorbed species is unaffected by the laser treatment. On the contrary, O$_a$ and O$_b$ follow opposite trends: the former increases while the latter decreases. The decrease of the O$_b$ component indicates the reduction of surface oxygen defects and/or adsorbed OH species [41]. The latter is likely due to the lower aspect ratio of the NRs which results into a smaller amount of surface available for adsorption. In the extreme case of surface smoothing, i.e. for the complete transition to a continuous film, the O$_b$ contribution is expected to be suppressed even more[55]. Both the surface smoothing and the reduction of surface defects enhance the carrier mobility and improve the conductivity of the system.

4.4.2. UPS

The average UPS spectra collected for the three samples are presented in the top panel of Fig.6 after background subtraction, and in the bottom panel of Fig.6 after further normalization to the Zn 3d peak. Three different features can be distinguished and are ascribable to the Zn 3d, to the O 2p hybridized states with Zn 4s and Zn 4p states, and to the O 2p (lone pair) states,
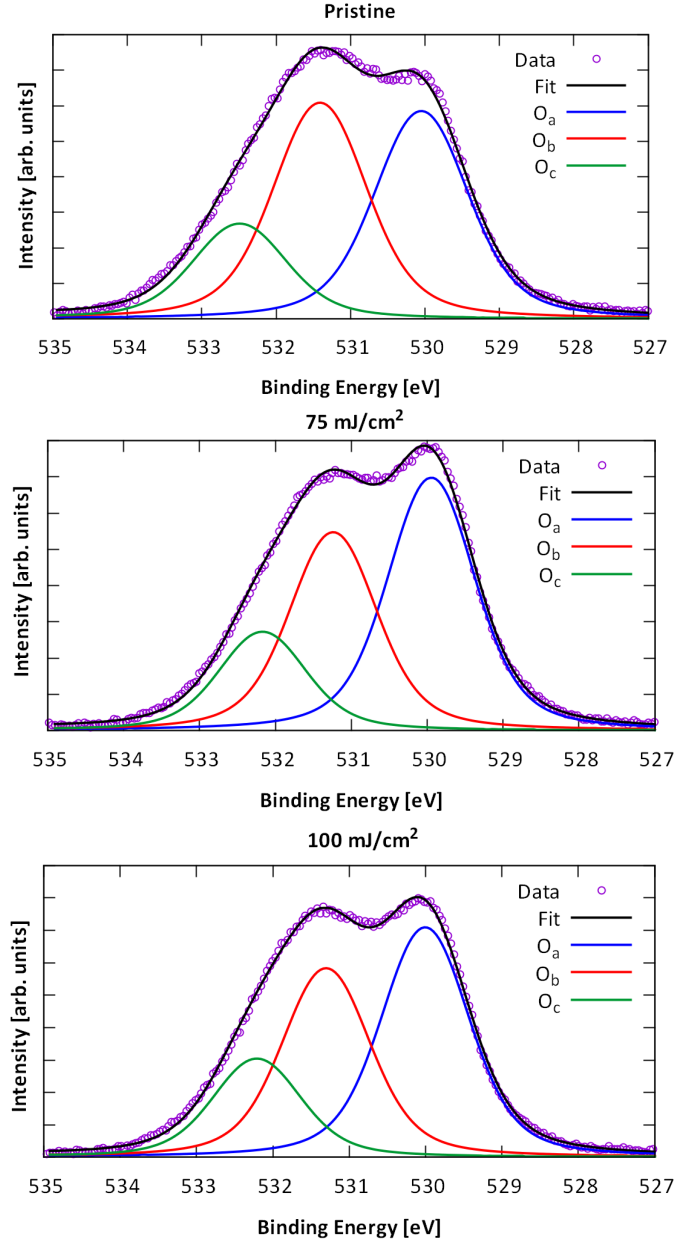

Figure 5: Results from the best fit of the O1s spectra for the three investigated samples. Data are shown after background subtraction.

approximately located at 11 eV, 8 eV and 6 eV respectively [56].

The overall intensity is higher for the irradiated samples (top panel Fig.6): as discussed for the XPS data, this can be explained with the lower concentration of adsorbed species and/or with the smoother surface. While the former affects mainly the oxygen-related peaks, the latter is expected to enhance all the three spectral features. Indeed, a smoother surface results into the reduction of the surface/volume ratio of the ZnO NRs and, as observed in the transition towards a film-like morphology[57], the three peaks gain in intensity. Although, as proved by our GIXD data, the ELA-induced structural rearrangement is limited to the topmost layers, the high surface sensitivity of photoelectron spectroscopies make the UPS spectra strongly affected by the morphological evolution.

The differences due to the ELA can be seen more clearly by comparing the spectra after normalization for the Zn 3d peak (bottom panel Fig.6). In particular, the Zn 3d peak is sharper, the O2p-Zn4s peak is weaker and the O2p peak stronger. All these behaviours are compatible with water desorption: indeed, a lower amount of adsorbed H_2O can account for the clearer visibility of the O 2p peak at 4.5 eV [53] and for the sharper nature of the Zn 3d peak around 11 eV, due to the suppression of a low energy component coming from Zn-OH [58]. This interpretation is also supported by the fact that the heavier effects, are found for the higher laser fluency and thus can be related to the surface smoothness. The surface smoothing induced by the ELA provides a smaller exposed surface where molecules could adsorb while, on the contrary, the high porosity of pristine sample favours the H_2O adsorption. Furthermore, the higher porosity hinders the water desorption during the mild annealing carried out before the measurements, thus yielding strong spectral differences. Even for the ELA samples, the mild annealing did not remove all the adsorbed H_2O molecules. In fact, the spectral features for all the measured samples showed a transient behaviour at the beginning of the data collection (see Fig.3 in the Supporting Information). This behaviour, lasting few minutes, is compatible with water desorption induced by the synchrotron beam. The spectra collected during the transition period were not considered in the calculations for the average signal per sample. The discussion reported above refers to the average signal obtained after the transient behaviour had stopped.

An additional consideration must be made about the Zn 3d peak. The increase in intensity and the suppression of its low energy component are compatible with the higher Zn concentration at the surface pointed out by GIXD and XPS.

A further effect of the ELA can be found in the steeper character of the right side of the O 2p peak, representing onset of the density of states. A linear extrapolation of the low binding energy (BE) edge of the spectra can be used to estimate the energy difference between the Fermi level, E_F, and the valence-band maximum, E_V, in the near-surface region [59]. The difference between the pristine and the irradiates samples is negligible, as shown in the inset of Fig.6: for all the samples, the $\Delta E \simeq 4.0$ eV. As the RT band gap of ZnO is 3.35 eV, the Fermi level of all our samples is in the conduction band, indicating a downward
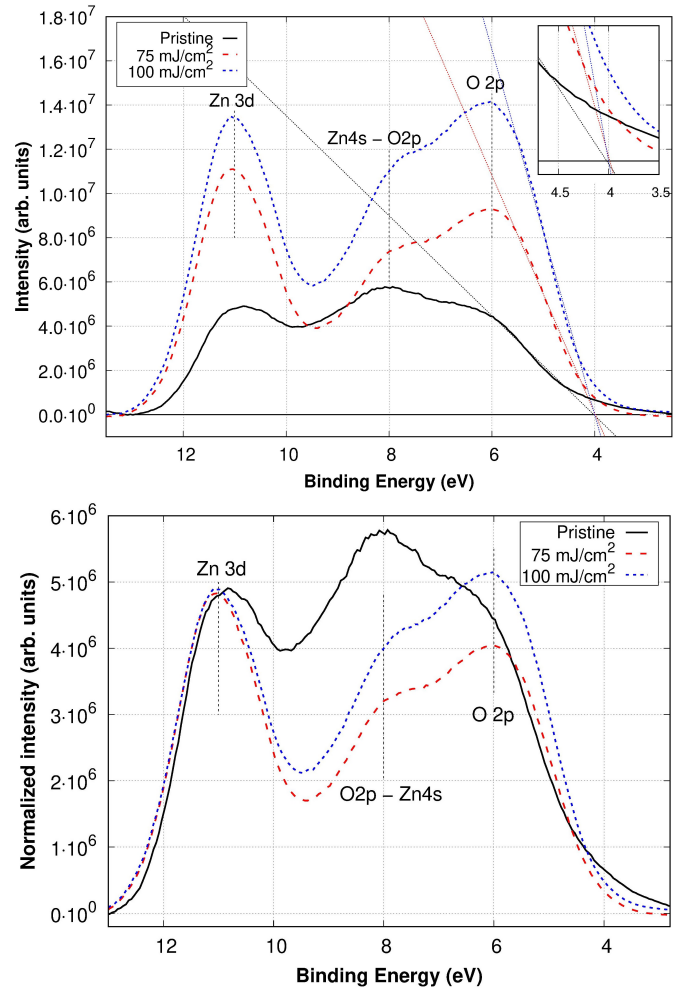

Figure 6: **Top** Average of the 10 UPS spectra collected on the pristine NRs (thick black line), and after the 75 (solid red line), and 100 mJ/cm^2 (dashed blue line) laser irradiation. The dashed lines show the results of the linear extrapolations of the leading edges on the low energy side of the spectra. **Bottom:** Average of the 10 UPS spectra collected on the pristine NRs (thick black line), and after the 75 (solid red line), and 100 mJ/cm^2 (dashed blue line) laser irradiation. Spectral intensities are normalised to the Zn 3d peaks for sake of comparison.

band bending and some electron accumulation at the surface [53]. The linear extrapolation indicates that the band bending is not affected by the ELA. Electron accumulation at the surface influences the charge mobility and, thus, can have strong repercussions on the overall conductivity. Noticeably, UPS data show no variations in the electron accumulation at least within the first 2÷3 nm from the surface. Henceforth, the charge mobility enhancement has to be ascribed to a different cause.

5. Conclusions

We have investigated the evolution of ZnO nanorods upon ELA at 75 and 100 mJ/cm^2. In particular, we explored the structural, optical, and electronic properties of the NRs.

From SEM images, it is clear that the laser heating induces the melting and further solidification of the topmost re-

gion. This leads to NRs presenting rounder tips and a lower height, pointing out an increase in the average layer density. GIXD showed that, upon laser exposure, the NRs preserve their wurtzite structure and that, in the tips region, both the average crystallite size and the lattice parameter decrease. This contraction is compatible with a transition towards a more metallic Zn environment at the surface.

An enhancement of the UV/visible emission ratio was observed through PL measurements. While the increase in the UV range can be explained with a Zn_i migration towards the surface, the origin of the decrease in the visible emission must be looked for in a deeper region of the gap. In particular, as the intensity of the visible emission is dominated by the surface defects, this is in agreement with the removal of the oxygen defects, occurring with the reduction of some ZnO at the very surface.

Upon irradiation, a significant increase in conductivity was found through TLM. Such increase, quantified by impedance spectroscopy, was found to reach a factor 4 for the higher laser fluence. The higher concentration of Zn at the surface could help in neutralising the negative charge accumulation at the surface, thus explaining the observed effect. Furthermore, the reduction of oxygen defects is also in agreement with the observed behaviour.

The interpretation of our results is supported by XPS data indicating the decrease of lattice oxygen at the surface and the increase of the Zn signal. UPS data, compatible with the Zn increase at the surface, are heavily affected by the water desorption from the surface and do not detect any significant band bending thus ruling out the possibility of lower electron accumulation.

Our exploration of the local effects induced by laser irradiation on ZnO NRs shows how the heating, although limited to the tip region, has a deep impact on the electronic and optical properties of the whole system, modifying the PL emission and raising the conductivity by three orders of magnitude. In the range investigated, the effects increase with the laser fluency. Our results confirm the model proposed for ZnO crystals and, to our knowledge, represent the first experimental evidence confirming the model about electronic properties of ZnO nanorods [29].

Acknowledgements

[1] D. Zhang, B. Gokce, and S. Barcikowski, Chemical reviews **117**, 3990 (2017).

[2] F. Spaepen, D. Turnbull, J. Poate, and J. W. Mayer, Laser Annealing of Semiconductors , 15 (1982).

[3] T. Sameshima, S. Usui, and M. Sekiya, IEEE Electron Device Letters **7**, 276 (1986).

[4] A. Voutsas, Applied Surface Science **208**, 250 (2003).

[5] W. S. Wong and A. Salleo, *Flexible electronics: materials and applications*, Vol. 11 (Springer Science & Business Media, 2009).

[6] A. Pecora, L. Maiolo, M. Cuscunà, D. Simeone, A. Minotti, L. Mariucci, and G. Fortunato, Solid-state electronics **52**, 348 (2008).

[7] V. Privitera, S. Scalese, A. La Magna, A. Pecora, M. Cuscunà, L. Maiolo, A. Minotti, D. Simeone, L. Mariucci, G. Fortunato, *et al.*, Journal of The Electrochemical Society **155**, H764 (2008).

[8] W. Cranton, N. Kalfagiannis, X. Hou, R. Ranson, D. Koutsogeorgis, *et al.*, Optics and Lasers in Engineering **80**, 45 (2016).

[9] K. Sera, F. Okumura, H. Uchida, S. Itoh, S. Kaneko, and K. Hotta, IEEE Transactions on Electron Devices **36**, 2868 (1989).

[10] S. Inoue, S. Utsunomiya, T. Saeki, and T. Shimoda, IEEE transactions on electron devices **49**, 1353 (2002).

[11] M. He, R. Ishihara, E. J. Neihof, Y. van Andel, H. Schellevis, W. Metselaar, and K. Beenakker, Japanese journal of applied physics **46**, 1245 (2007).

[12] M. Nakata, K. Takechi, S. Yamaguchi, E. Tokumitsu, H. Yamaguchi, and S. Kaneko, Japanese Journal of Applied Physics **48**, 115505 (2009).

[13] E. Yarali, C. Koutsiaki, H. Faber, K. Tetzner, E. Yengel, P. Patsalas, N. Kalfagiannis, D. C. Koutsogeorgis, and T. D. Anthopoulos, Advanced Functional Materials , 1906022 (2019).

[14] H. Palneedi, J. H. Park, D. Maurya, M. Peddigari, G.-T. Hwang, V. Annapureddy, J.-W. Kim, J.-J. Choi, B.-D. Hahn, S. Priya, *et al.*, Advanced Materials **30**, 1705148 (2018).

[15] G. Fiaschi, S. Mirabella, G. Franzò, L. Maiolo, A. Chitu, Y. Komem, and Y. Shacham-Diamand, Applied Surface Science **458**, 800 (2018).

[16] J. Maeng, S. Heo, G. Jo, M. Choe, S. Kim, H. Hwang, and T. Lee, Nanotechnology **20**, 095203 (2009).

[17] H. Pan, S. H. Ko, N. Misra, and C. P. Grigoropoulos, Applied physics letters **94**, 071117 (2009).

[18] M.-Y. Pu, J.-Z. Chen, and I.-C. Cheng, Ceramics International **39**, 6183 (2013).

[19] A. Manekkathodi, M.-Y. Lu, C. W. Wang, and L.-J. Chen, Advanced materials **22**, 4059 (2010).

[20] S. Baruah and J. Dutta, Science and technology of advanced materials **10**, 013001 (2009).

[21] S. Ju, A. Facchetti, Y. Xuan, J. Liu, F. Ishikawa, P. Ye, C. Zhou, T. J. Marks, and D. B. Janes, Nature nanotechnology **2**, 378 (2007).

[22] J. Hasnidawani, H. Azlina, H. Norita, N. Bonnia, S. Ratim, and E. Ali, Procedia Chemistry **19**, 211 (2016).

[23] O. Katz, G. Bahir, and J. Salzman, Applied physics letters **84**, 4092 (2004).

[24] M. Nie, Y. Zhao, and Y. Zeng, Journal of Laser Applications **26**, 022005 (2014).

[25] Y. Zhao and Y. Jiang, Journal of Applied Physics **103**, 114903 (2008).

[26] T. Lin, C. Huang, G. Shu, J. Shen, C. Hsiao, and S.-Y. Chen, physica status solidi (a) **209**, 1461 (2012).

[27] J. C. Moore and C. V. Thompson, Sensors **13**, 9921 (2013).

[28] E. Barbagiovanni, R. Reitano, G. Franzò, V. Strano, A. Terrasi, and S. Mirabella, Nanoscale **8**, 995 (2016).

[29] J. Kaupužs, A. Medvids, P. Onufrijevs, and H. Mimura, Optics & Laser Technology **111**, 121 (2019).

[30] D. Polese, I. Lucarini, A. Convertino, F. Maita, G. Fortunato, and L. Maiolo, in *2019 IEEE SENSORS* (IEEE, 2019) pp. 1–4.

[31] G. Fiaschi, S. Cosentino, R. Pandey, S. Mirabella, V. Strano, L. Maiolo, D. Grandjean, P. Lievens, and Y. Shacham-Diamand, Journal of Electroanalytical Chemistry **811**, 89 (2018).

[32] J. R. Plaisier, L. Nodari, L. Gigli, E. P. R. San Miguel, R. Bertoncello, and A. Lausi, Acta Imeko **6**, 71 (2017).

[33] H.-K. Kim, T.-Y. Seong, K.-K. Kim, S.-J. Park, Y. S. Yoon, and I. Adesida, Japanese journal of applied physics **43**, 976 (2004).

[34] A. Abrami, M. Barnaba, L. Battistello, A. Bianco, B. Brena, G. Cautero, Q. Chen, D. Cocco, G. Comelli, S. Contrino, *et al.*, Review of scientific instruments **66**, 1618 (1995).

[35] L. Petaccia, P. Vilmercati, S. Gorovikov, M. Barnaba, A. Bianco, D. Cocco, C. Masciovecchio, and A. Goldoni, Nuclear Instruments and Methods in Physics Research Section A: Accelerators, Spectrometers, Detectors and Associated Equipment **606**, 780 (2009).

[36] X. Li, Y. Wang, W. Liu, G. Jiang, and C. Zhu, Materials Letters **85**, 25 (2012).

[37] S. A. Ansari, M. M. Khan, S. Kalathil, A. Nisar, J. Lee, and M. H. Cho,

Nanoscale **5**, 9238 (2013).

[38] S. Cho, J. Ma, Y. Kim, Y. Sun, G. K. Wong, and J. B. Ketterson, Applied Physics Letters **75**, 2761 (1999).

[39] P. Scherrer and N. Gottingen, Math-Pys. Kl. **2**, 96 (1918).

[40] A. B. Djurišić, W. C. Choy, V. A. L. Roy, Y. H. Leung, C. Y. Kwong, K. W. Cheah, T. Gundu Rao, W. K. Chan, H. Fei Lui, and C. Surya, Advanced Functional Materials **14**, 856 (2004).

[41] H. Mosbacker, Y. Strzhemechny, B. White, P. Smith, D. C. Look, D. Reynolds, C. Litton, and L. Brillson, Applied Physics Letters **87**, 012102 (2005).

[42] T. Shimogaki, K. Okazaki, D. Nakamura, M. Higashihata, T. Asano, and T. Okada, Optics express **20**, 15247 (2012).

[43] S. Studenikin and M. Cocivera, Journal of Applied Physics **91**, 5060 (2002).

[44] M. Allen, C. Swartz, T. Myers, T. Veal, C. McConville, and S. Durbin, Physical Review B **81**, 075211 (2010).

[45] I. Grohmann, B. Peplinski, and W. Unger, Surface and interface analysis **19**, 591 (1992).

[46] C. Wagner, W. Riggs, L. Davis, J. Moulder, and G. Muilenberg, Google Scholar , 298 (2006).

[47] S. Bai, T. Guo, Y. Zhao, R. Luo, D. Li, A. Chen, and C. C. Liu, Journal of Materials Chemistry A **1**, 11335 (2013).

[48] R. Gurwitz, R. Cohen, and I. Shalish, Journal of Applied Physics **115**, 033701 (2014).

[49] J. Lee, J. Chung, and S. Lim, Physica E: Low-dimensional Systems and Nanostructures **42**, 2143 (2010).

[50] T. Herng, S. Lau, S. Yu, H. Yang, K. Teng, and J. Chen, Journal of Physics: Condensed Matter **19**, 236214 (2007).

[51] J. Pilz, A. Perrotta, P. Christian, M. Tazreiter, R. Resel, G. Leising, T. Griesser, and A. M. Coclite, Journal of Vacuum Science & Technology A: Vacuum, Surfaces, and Films **36**, 01A109 (2018).

[52] K. Tam, C. Cheung, Y. Leung, A. Djurišić, C. Ling, C. Beling, S. Fung, W. Kwok, W. Chan, D. Phillips, *et al.*, The Journal of Physical Chemistry B **110**, 20865 (2006).

[53] M. J. Al-Saadi, S. H. Al-Harthi, H. H. Kyaw, M. T. Myint, T. Bora, K. Laxman, A. Al-Hinai, and J. Dutta, Nanoscale research letters **12**, 22 (2017).

[54] M. Chen, X. Wang, Y. Yu, Z. Pei, X. Bai, C. Sun, R. Huang, and L. Wen, Applied Surface Science **158**, 134 (2000).

[55] P.-T. Hsieh, Y.-C. Chen, K.-S. Kao, and C.-M. Wang, Applied Physics A **90**, 317 (2008).

[56] N. M. Schmerl, A. R. Gentle, J. S. Quinton, G. B. Smith, and G. G. Andersson, The Journal of Physical Chemistry C **120**, 15772 (2016).

[57] J. Chiou, K. K. Kumar, J. Jan, H. Tsai, C. Bao, W.-F. Pong, F. Chien, M.-H. Tsai, I.-H. Hong, R. Klauser, *et al.*, Applied physics letters **85**, 3220 (2004).

[58] M. Bär, J. Reichardt, A. Grimm, I. Kötschau, I. Lauermann, K. Rahne, S. Sokoll, M. Lux-Steiner, C.-H. Fischer, L. Weinhardt, *et al.*, Journal of applied physics **98**, 053702 (2005).

[59] S. A. Chambers, T. Droubay, T. C. Kaspar, and M. Gutowski, Journal of Vacuum Science & Technology B: Microelectronics and Nanometer Structures Processing, Measurement, and Phenomena **22**, 2205 (2004).

Declaration of interests

☒ The authors declare that they have no known competing financial interests or personal relationships that could have appeared to influence the work reported in this paper.

☐The authors declare the following financial interests/personal relationships which may be considered as potential competing interests:
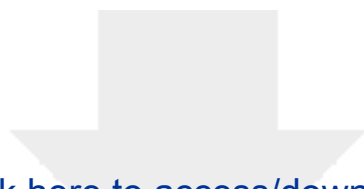
Click here to access/download

Supplementary Material for on-line publication only
ZnO_supp-info.pdf